Electronic Supplementary Material (ESI)

Insights into the decomposition of zirconium acetylacetonate using synchrotron radiation: Routes to the formation of volatile Zr-intermediates

Sebastian Grimm[a,b], Seung-Jin Baik[b,c], Patrick Hemberger[d], Tina Kasper[b,e], Andreas Kempf[b,c] and Burak Atakan[a,b]*

[a] IVG, Institute for Combustion and Gas Dynamics – Chair of Thermodynamics, University of Duisburg-Essen, 47057, Germany
[b] CENIDE, Center for Nanointegration Duisburg-Essen, University of Duisburg-Essen, 47057, Germany
[c] IVG, Institute for Combustion and Gas Dynamics - Chair of Fluid Dynamics, University of Duisburg-Essen, 47057, Germany
[d] Laboratory for Synchrotron Radiation and Femtochemistry, Paul Scherrer Institute, CH-5232 Villigen-PSI, Switzerland
[e] IVG, Institute for Combustion and Gas Dynamics – Mass Spectrometry in Reacting Flows, University of Duisburg-Essen, 47057, Germany

*Corresponding author. E-mail address: sebastian.grimm@uni-due.de (S. Grimm)

ORCID IDs:

0000-0002-7378-3224 (S. Grimm)

0000-0002-3362-5424 (S.-J. Baik)

0000-0002-1251-4549 (P. Hemberger)

0000-0003-3993-5316 (T. Kasper)

0000-0003-3627-4524 (Andreas M. Kempf)

0000-0002-1361-8315 (B. Atakan)

S 1 Numerical modelling of the microreactor

S 1.1 Governing equations

The Reynolds-averaged Navier-Stokes (RANS) equations contain mass and momentum conservations written as:

$$\frac{\partial \rho}{\partial t} + \frac{\partial}{\partial x_i}(\rho \bar{u}_i) = 0 \quad \textbf{(E1)}$$

$$\frac{\partial}{\partial t}(\rho \bar{u}_i) + \frac{\partial}{\partial x_j}(\rho \bar{u}_i \bar{u}_j) = -\frac{\partial p}{\partial x_j} + \frac{\partial}{\partial x_j}\left[\mu\left(\frac{\partial u_i}{\partial x_j} + \frac{\partial u_j}{\partial x_i}\right) - \rho\overline{u_i' u_j'}\right] \quad \textbf{(E2)}$$

, where μ is the dynamic viscosity. The velocity was decomposed with time-averaged component $\bar{u}_i$ and fluctuating component u_i', as $u_i = \bar{u}_i + u_i'$.

In the present work, based on the observed flow characteristic in the previous study [1], the RANS equations combined with a slip (boundary) condition were used to investigate the flow in the microreactor under the given conditions relevant to interpret the experimental data.

For the slip boundary implementation in the simulation, a simple model for the slip fluid velocity at the wall was used, which can be expressed as:

$$\boldsymbol{V}_{slip} = l_s \left.\frac{\partial \boldsymbol{V}}{\partial \boldsymbol{n}}\right|_{at\ wall} \quad \textbf{(E3)}$$

, where l_s is the slip length and *n* denotes the normal vector to the wall. In the present work, the slip length l_s is calculated using the approach suggested by Morris et al. [2]:

$$l_s = \alpha \cdot L \cdot Kn \quad \textbf{(E4)}$$

Where the local Knudsen number *Kn* is defined with the Mach number *M* and Reynolds number *Re* as: $Kn = (\sqrt{\gamma\pi}M)/(\sqrt{2}Re)$ [3]. The model constant α in eq. E4 was suggested to be 1.15 [2] and the diameter of the microreactor was used as the characteristic length *L*.

S 1.2 Numerical domain and boundary conditions

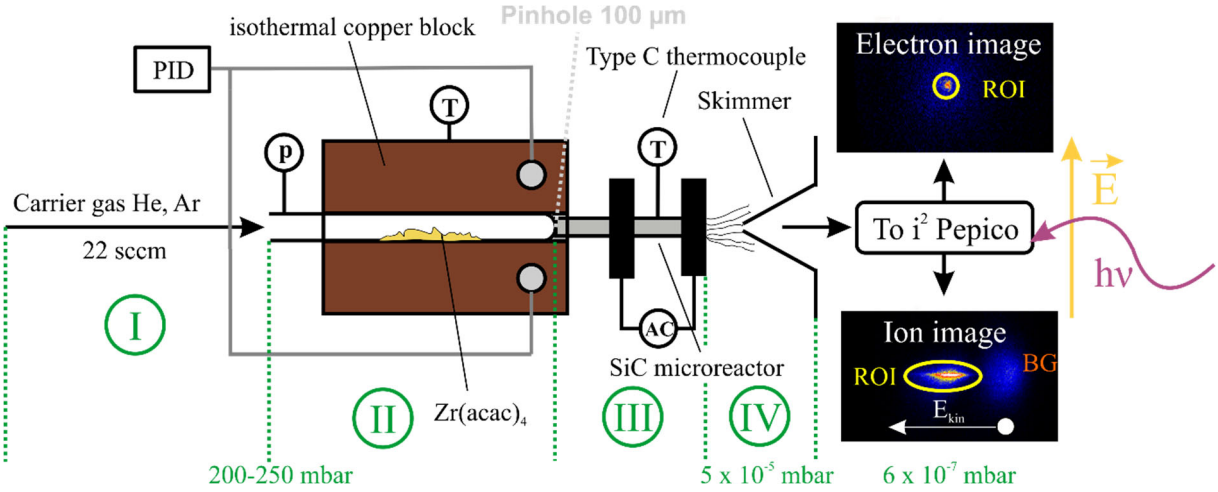

Figure S 1 Schematic sketch of the experimental setup, based on [3]. The boundary conditions applied for the numerical simulation are displayed in green Roman numerals and are summarized in **Table S 1**.

Table S 1 Boundary conditions for the CFD simulation of the microreactor. Roman numerals are in accordance with **Figure S 1**.

Nr.	Boundary type	Pressure mbar	Temperature K
I	Inlet	214	293
II	No-slip wall	-	403
III	Slip wall	-	Helium: 423-903 (12 points) – Argon: 423, 671, 803
IV	Outlet	5×10^{-5}	-

S 1.3 Comparison of the temperature profiles using different dilution gases

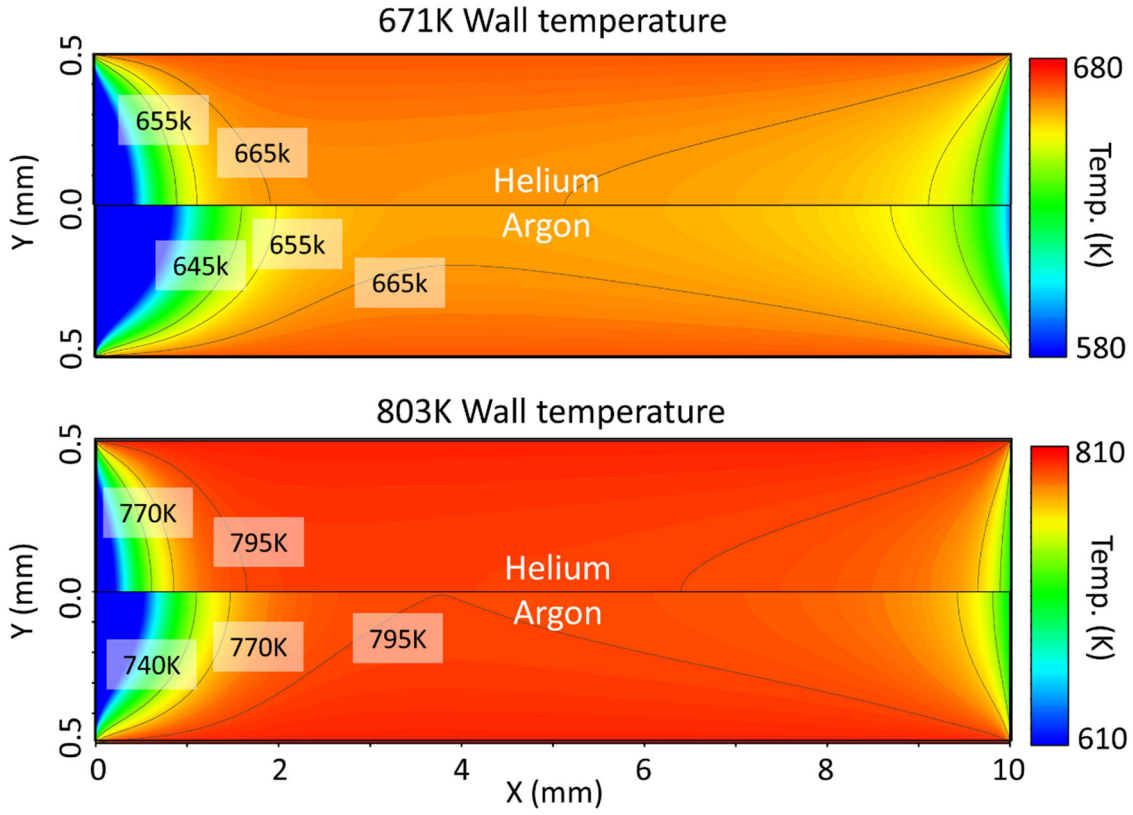

Figure S 2 Contour plots of the reactor temperature field obtained from CFD calculations in helium (top side) and argon (bottom side) at surface temperatures of 671 and 803 K, where most of the intermediate species were observed upon pyrolysis of $Zr(acac)_4$.

In order to correctly interpret the temperature onset of the formation of the detected intermediate species and interpret the chemical pathways to their formation more precisely, we performed two different simulation sets with the same boundary conditions, but using helium and argon as dilution gas. Considering the flow field, the main difference between helium and argon can be explained by a higher heat conductivity of helium, which in turn is responsible for more efficient heat transfer in the reactor by conduction and convection and therefore leads to a more plug-flow like temperature profile in the microreactor. Additionally, we found, that a lower inlet pressure (here ca. 2.14×10^4 Pa) leads to a more uniform temperature profile in comparison to the results obtained in our previous study (ca. 1.6×10^5 Pa), since the density of the gas is 6 times smaller [1]. This should lead to an increase in signal intensity, as well as an accurate interpretation of the temperature-dependence of the collected experimental data with respect to chemical mechanisms and kinetics.

S 1.4 Flow field in the microreactor

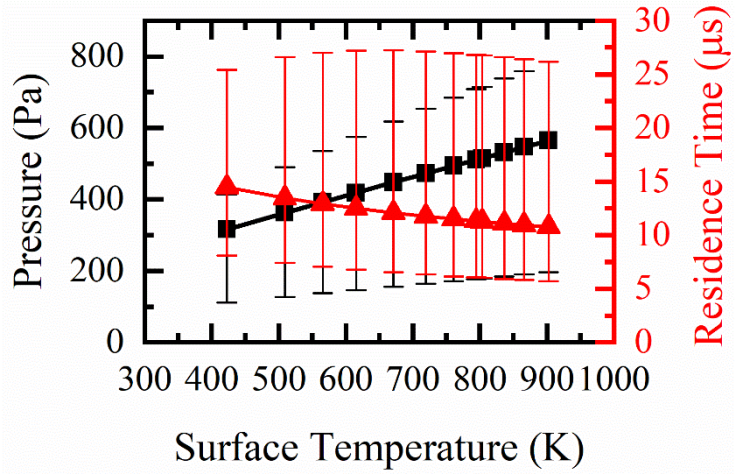

Figure S 3 Averaged pressure and residence time inside the heated area as a function of surface temperature using helium as dilution gas. The error bars indicate the maximum and minimum values along the axial centerline of the microreactor.

Figure S 3 shows the averaged pressure and residence time for the heated zone (10 mm length) from each simulation with surface temperatures ranging from 400 to 900 K, which correspond to the measured values in the experiment. Pressure and residence time profiles show an almost linear course upon a variation of the surface temperature. We report here average residence times of 10.5 ~ 14.5 µs in the case of helium used as dilution gas, which is in accordance with previous studies that hint on the beneficial properties of helium for the derivation of reaction kinetics in such small pyrolysis reactors [4–6].

S 2 Precursor stability at room temperature

S 2.1 Dissociative ionization

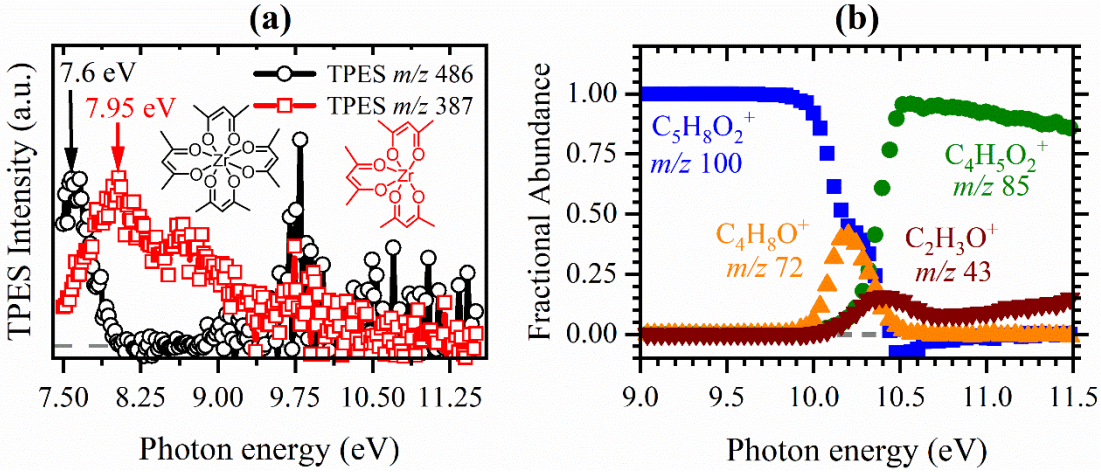

Figure S 4 (a) Mass-selected threshold photoelectron spectra (ms-TPES) recorded at room temperature in the 7.5–11.4 eV photon energy range. The main dissociative ionization product at *m/z* 387 is denoted in red, whereas the parent molecule $Zr(C_5H_7O_2)_4$ is shown in black along with the vertical ionization energies; **(b)** Breakdown diagram of $C_5H_8O_2$ at 403 K shows the dissociative ionization of acetylacetone.

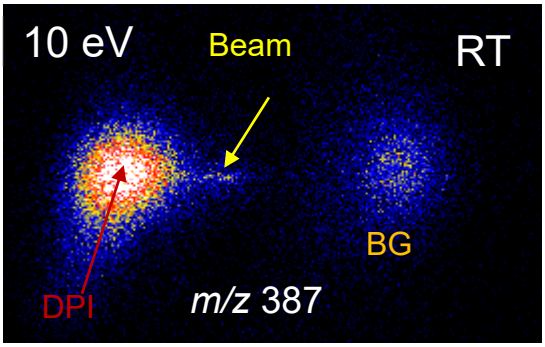

Figure S 5 Room temperature ion image of *m/z* 387 at an evaporator temperature of 403 K and a photon energy of 10 eV. A broad kinetic energy distribution hints that *m/z* 387 ($Zr(acac)_3^+$) is the main fragment formed by dissociative ionization of $Zr(acac)_4$.

S 2.2 Threshold photoelectron spectrum of acetic acid (*m/z* 60)

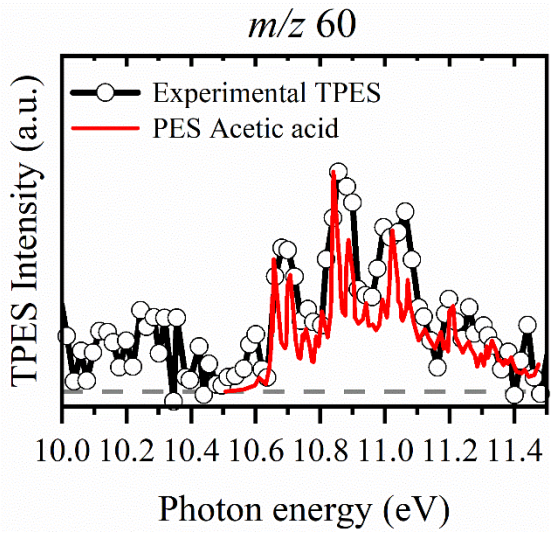

Figure S 6 Threshold photoelectron spectrum of *m/z* 60 at an evaporator temperature of 403 K (black symbols and line). The literature reference spectrum of $C_2H_3O_2$ (acetic acid) [7] is shown in red and is in good agreement with the bands observed here.

S 3 Species assignment of minor decomposition products

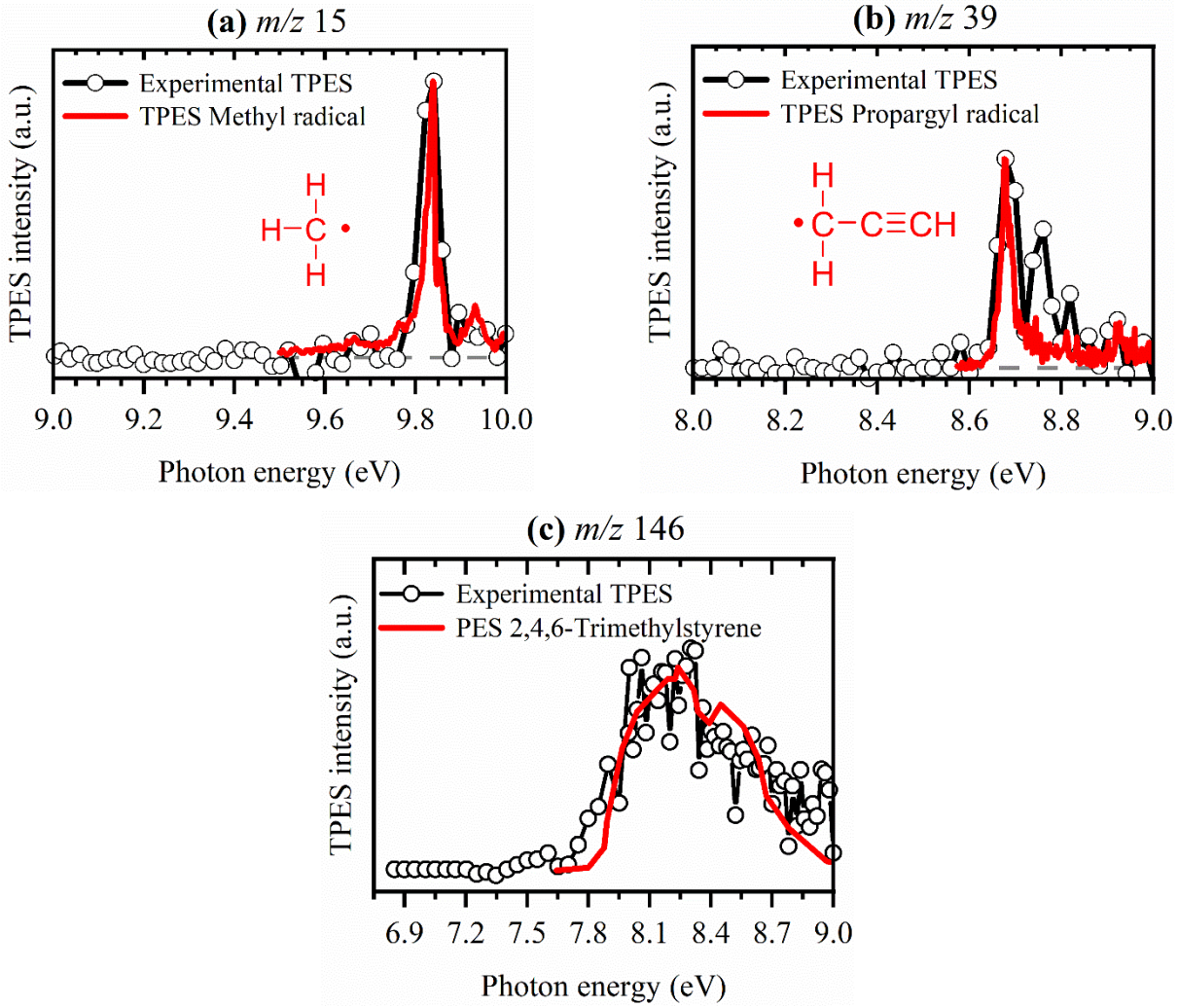

Figure S 7 ms-TPE spectra of minor decomposition products at a temperature of 803 K (a) and (b) and 776 K (c). Literature references in red are as follows: **(a)** *m/z* 15 Methyl radical (CH_3) [8]; **(b)** *m/z* 39 Propargyl radical (C_3H_3) [9] and **(c)** *m/z* 146 2,4,6-Trimethylstyrene ($C_{11}H_{14}$) [10].

S4 Velocity map images of some of the detected Zr-species

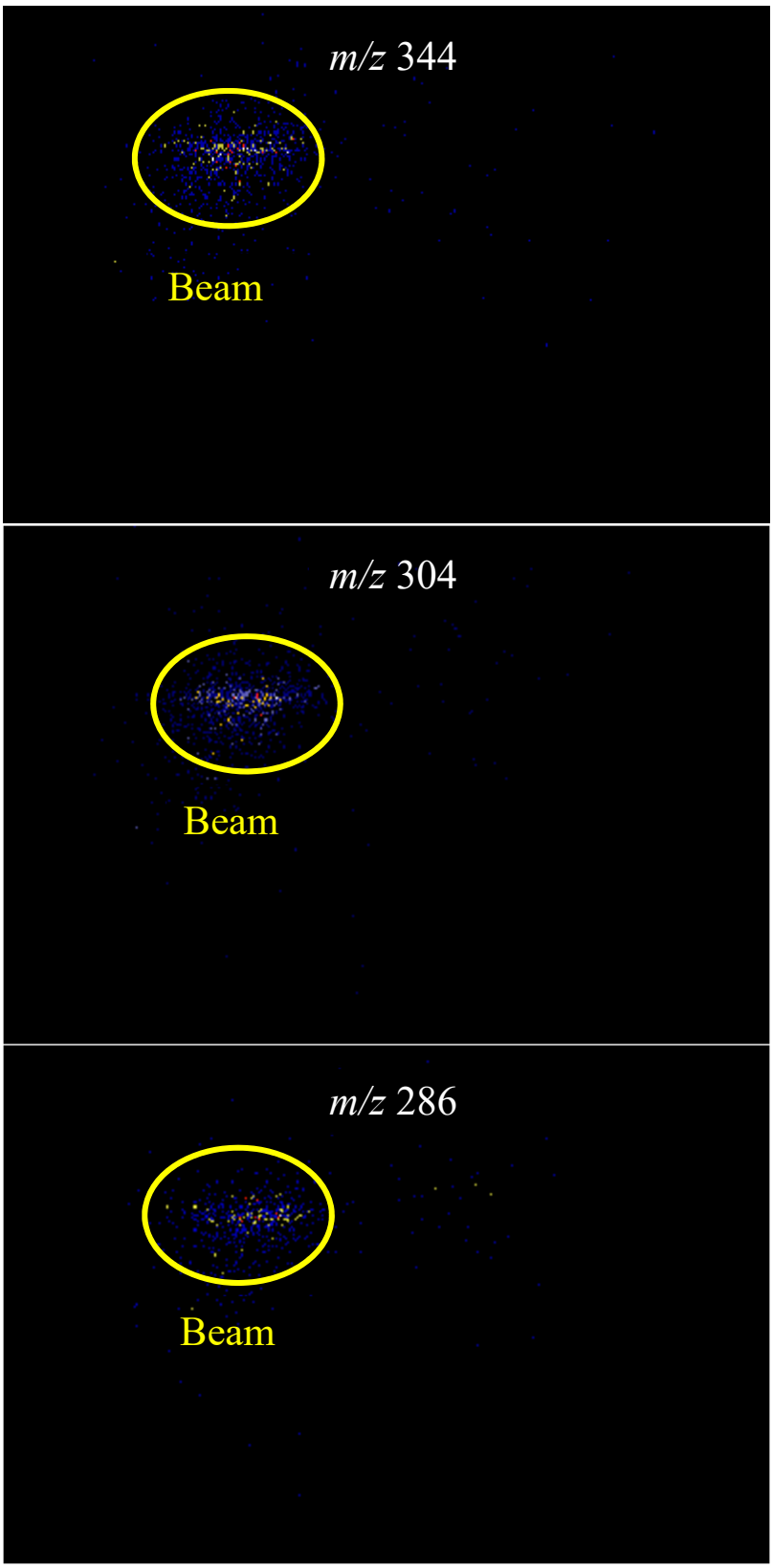

Figure S 8 Ion velocity map images of the most abundant Zr-species *m/z* 344, 304 and 286 at a temperature of 776 K, recorded at 8.5 eV.

References

[1] S. Grimm, S.-J. Baik, P. Hemberger, A. Bodi, A.M. Kempf, T. Kasper, B. Atakan, Physical chemistry chemical physics PCCP 23 (2021) 15059–15075.

[2] D.L. Morris, L. Hannon, A.L. Garcia, Physical review. A, Atomic, molecular, and optical physics 46 (1992) 5279–5281.

[3] G. Karniadakis, Microflows and nanoflows: Fundamentals and simulation, Springer, New York, NY, 2005.

[4] Q. Guan, K.N. Urness, T.K. Ormond, D.E. David, G. Barney Ellison, J.W. Daily, International Reviews in Physical Chemistry 33 (2014) 447–487.

[5] P.J. Weddle, C. Karakaya, H. Zhu, R. Sivaramakrishnan, K. Prozument, R.J. Kee, Int. J. Chem. Kinet. 50 (2018) 473–480.

[6] M.V. Zagidullin, R.I. Kaiser, D.P. Porfiriev, I.P. Zavershinskiy, M. Ahmed, V.N. Azyazov, A.M. Mebel, The journal of physical chemistry. A 122 (2018) 8819–8827.

[7] W. von Niessen, G. Bieri, L. Åsbrink, Journal of Electron Spectroscopy and Related Phenomena 21 (1980) 175–191.

[8] B.K. Cunha de Miranda, C. Alcaraz, M. Elhanine, B. Noller, P. Hemberger, I. Fischer, G.A. Garcia, H. Soldi-Lose, B. Gans, L.A.V. Mendes, S. Boyé-Péronne, S. Douin, J. Zabka, P. Botschwina, The journal of physical chemistry. A 114 (2010) 4818–4830.

[9] P. Hemberger, M. Lang, B. Noller, I. Fischer, C. Alcaraz, B.K. Cunha de Miranda, G.A. Garcia, H. Soldi-Lose, The journal of physical chemistry. A 115 (2011) 2225–2230.

[10] T. Kobayashi, S. Nagakura, Journal of Electron Spectroscopy and Related Phenomena 7 (1975) 488–491.